World Journal for Pediatric and Congenital Heart Surgery

The Enduring Impact of Shape Following Perfect Aortic Coarctation Repair

Journal:	*World Journal for Pediatric and Congenital Heart Surgery*
Manuscript ID	WJPCHS-24-0065.R2
Manuscript Type:	Original Article
Date Submitted by the Author:	21-Jun-2024
Complete List of Authors:	Swanson, Liam; University College London, Institute of Cardiovascular Science Sauvage, Emilie; University College London, Institute of Cardiovascular Science Ngoepe, Malebogo; University of Cape Town, Department of Mechanical Engineering Schievano, Silvia; University College London, Institute of Cardiovascular Science Bruse, Jan; Vicomtech Foundation, Basque Research Technology Alliance (BRTA) Hsia, T-Y; Arnold Palmer Hospital for Children, Pediatric Cardiac Surgery
Keywords:	Coarctation of the aorta, statistical shape modelling, computational fluid dynamics, viscous energy loss, long term outcome
Abstract:	Objectives Aortic arch appearances are associated with worse cardiac function and chronic hypertension late after aortic coarctation repair, even without residual obstruction. Statistical shape modeling (SSM) identified specific 3D arch shapes linked to poorer cardiovascular outcomes. We sought a mechanistic explanation. Methods From 53 asymptomatic patients late after aortic coarctation repair with no residual obstruction (age:22.3 ± 5.6 years; 12-38 years after operation), 8 arch shapes associated with 4 best and 4 worst cardiovascular parameters were obtained from 3D SSM. 4 favorable shapes were affiliated with LV ejection fraction +2 standard deviation (SD) from the mean, and indexed LV end diastolic volume/indexed LV mass/resting systolic blood pressure that were -2SD. 4 unfavorable shapes were defined by the reverse. Computational Fluid Dynamics modeling was carried out to assess differences in pressure gradient across the arch and viscous energy loss (VEL) between favorable and unfavorable aortic arches. Results In all aortic arches, the pressure gradients were clinically insignificant (<8 mmHg). However, in the 4 unfavorable aortic arches, VEL were uniformly higher than those in the favorable shapes (VEL difference: 15-32%). There was increased turbulence and more complex propagation of VEL along the unfavorable aortic arches.

	Conclusions This study reveals the variable flow dynamics that underpins the association of aortic arch shapes with worse cardiovascular outcomes late after successful aortic coarctation repair. Higher VEL persist in the unfavorable aortic arch shapes. Further understanding of the mechanism of VE results in cardiovascular maladaptation may afford mitigating strategies to monitor and modify this unrelenting liability.

The Enduring Impact of Shape Following Perfect Aortic Coarctation Repair

Liam Swanson, MSc,[1] Emilie Sauvage, PhD,[1] Malebogo Ngoepe, PhD,[2] Silvia Schievano, PhD,[1] Jan L. Bruse, PhD,[3] Tain-Yen Hsia, MD, MSc[4]

[1] University College London, Institute of Cardiovascular Science & Great Ormond Street Hospital for Children, London, United Kingdom

[2] University of Cape Town, Department of Mechanical Engineering, Cape Town, South Africa

[3] Vicomtech Foundation, Basque Research Technology Alliance (BRTA), Donostia-San Sebastián, Spain

[4] Heart Center at Arnold Palmer Hospital for Children, Orlando, FL, USA

Short Title:

Aortic arch after coarctation repair

COI Statement

No author has a conflict of interest to declare.

Corresponding Author Contact Information

Tain-Yen Hsia, MD. tyhsia@me.com

Meeting Presentation

The manuscript was previously presented at the 49th Annual Meeting of the Congenital Heart Surgeons' Society, October 23-24, 2022, in Chicago, Illinois.

Article Word Count

4467

Abstract

Objectives

Aortic arch appearances are associated with worse cardiac function and chronic hypertension late after aortic coarctation repair, even without residual obstruction. Statistical shape modeling (SSM) identified specific 3D arch shapes linked to poorer cardiovascular outcomes. We sought a mechanistic explanation.

Methods

From 53 asymptomatic patients late after aortic coarctation repair with no residual obstruction (age:22.3 ± 5.6 years; 12-38 years after operation), 8 arch shapes associated with 4 best and 4 worst cardiovascular parameters were obtained from 3D SSM. 4 favorable shapes were affiliated with LV ejection fraction +2 standard deviation (SD) from the mean, and indexed LV end diastolic volume/indexed LV mass/resting systolic blood pressure that were -2SD. 4 unfavorable shapes were defined by the reverse. Computational Fluid Dynamics modeling was carried out to assess differences in pressure gradient across the arch and viscous energy loss (VEL) between favorable and unfavorable aortic arches.

Results

In all aortic arches, the pressure gradients were clinically insignificant (<8 mmHg). However, in the 4 unfavorable aortic arches, VEL were uniformly higher than those in the favorable shapes (VEL difference: 15-32%). There was increased turbulence and more complex propagation of VEL along the unfavorable aortic arches.

Conclusions

This study reveals the variable flow dynamics that underpins the association of aortic arch shapes with worse cardiovascular outcomes late after successful aortic coarctation repair. Higher VEL

persist in the unfavorable aortic arch shapes. Further understanding of the mechanism of VE results in cardiovascular maladaptation may afford mitigating strategies to monitor and modify this unrelenting liability.

(Word Count: 250)

Keywords

Coarctation of the aorta; statistical shape modelling; computational fluid dynamics; viscous energy loss

Glossary of Abbreviations

2D	=	2-Dimensional
3D	=	3-Dimensional
BP	=	Blood Pressure
CFD	=	Computational Fluid Dynamics
CMR	=	Cardiovascular Magnetic Resonance
CoA	=	Coarctation of the Aorta
iLVEDV	=	indexed Left Ventricular End Diastolic Volume
iLVM	=	indexed Left Ventricular Mass
LVEF	=	Left Ventricular Ejection Fraction
PLS	=	Partial Least Squares
SSM	=	Statistical Shape Model

Introduction

Coarctation of the aorta (CoA) is a lesion with well-established surgical and interventional approaches for correction.[1-2] However, despite undergoing a 'successful' repair with good early outcomes, many patients with CoA face late complications and morbidities, including medically refractory hypertension, reduced heart function, and exercise capacity.[3-5] While the etiology for these challenges is likely to be multi-factorial, an awareness is emerging that the aortic arch shape, long after initial repair, may be an important mechanistic contributor.[6-9] To overcome the limitation of using 2-dimensional (2D), i.e. heigh-width ratio or angulation, to describe the 3-dimensional (3D) aortic arch,[10-13] we reported using statistical shape modelling (SSM) to leverage large medical imaging datasets to assess a *population* of aortic arch anatomies in 3D space.[14-15] These studies reveal specific 3D aortic arch shapes associated with worse cardiac function/hypertension late after CoA repair (Figure 1).[16-17]

To further understand *how* 3D aortic arch shape can impact late cardiac outcomes in patients without residual aortic arch obstruction or clinically relevant arch pressure gradients, we adopted novel computational fluid dynamics (CFD) modelling in conjunction with the SSM phenomenological approach. We hypothesise that unique mechanistic metrics, gleaned from CFD, are associated with those aortic arch shape features linked to previously reported unfavorable late cardiac function.[17]

Materials and Methods

Geometry

The analysis is based on the shape modes generated by the SSM, as previously reported, from 53 asymptomatic patients late after isolated *surgical* CoA repair (age = 22.3 ± 5.6 years; 12 to 38 years after initial operation) with no clinically important residual obstruction or stenosis.[17] We analyzed routine follow-up CMR imaging data (1.5T Avanto MR scanner, Siemens Medical Solutions, Germany) of 53 asymptomatic patients late following isolated aortic coarctation repair (CoA; mean age 22.3±5.6 years), including scans from 2007 to 2015. The CMRs were obtained 12 to 38 years (mean 20.6±5.0 years) following initial CoA repair, and none had hemodynamically significant residual aortic arch obstruction or CoA requiring revision/reintervention as determined by Doppler echocardiographic interrogation. 36 patients had initial repair during the first year of life (68%), 7 patients in second year, and 10 patients more than 5 years after birth (with the oldest age at repair at 10 years). Patients with additional left-sided obstructive lesion (including hypoplastic left heart syndrome) or hypoplastic aortic arch/interrupted aortic arch were excluded, as well as those with aneurysmal dilatation and those with imaging artifacts due to stents or valve prosthesis. Approximately 80% of the cohort had an end-to-end (E-E) CoA repair, while nearly half had a bicuspid aortic valve (Table 1). Ethical approval was obtained for the use of image data for research, and all patients or legal guardians gave informed consent.

For each of the 4 cardiac function parameters (LVEF, iLVEDV, iLVM and BP), 2 unique aortic arch shapes are extracted from PLS to match high (+2SD) or low (-2SD) cardiac function values. For example, for LVEF, an aortic arch shape associated with LVEF that is +2 SD from the cohort mean is obtained, along with one associated with LVEF that is -2 SD from the mean. Thus, 4 pairs

(or 8 total) of aortic arch shapes were generated, and further post-processed using the Vascular Modelling Toolkit (VMTK) software (Orobix, Bergamo, Italy) to prepare for CFD modelling.[18]

Pipe-like flow extensions were added at the transverse aortic arch sections (Figure 2A) to account for the volume of flow through the head and neck vessels. Flow extensions, of length 0.5 and 10 times their diameters, were added to the inlet and outlets of each geometry, respectively, to avoid recirculation at the outlets and allow boundary condition imposition at the inlet. An example of the resulting processed shapes is shown in Figure 2.

CFD

All 8 geometries were meshed using ANSYS Integrated Computer Engineering Modelling for Computational Fluid Dynamics (ANSYS Inc., Canonsburg, PA) software package and simulations were carried out in ANSYS Fluent v19.0. Post-processing and result analysis were conducted in ParaView v5.9.0 (Kitware, New York). The computational mesh comprised tetrahedral cells in the lumen of the aorta and thin prismatic cells in the near-wall region. Mesh sensitivity analysis that confirmed independence with ~2 million cells and error of <2% is detailed in the Supplementary Material.

A transient parabolic inlet velocity profile was adapted from literature,[19] obtained from phase contrasted CMR for a patient with a healthy aorta. Through linear scaling, the volumetric flow rate plot (Fig. 2) was generated for a peak volumetric flow rate of 400 ml/s, at 0.11s, for CoA patients post-repair.[20] Cardiac cycle was 1s which corresponds to a heart rate of 60 BPM.

Like previously studies,[21] outlet boundary conditions were defined as flow, where the total inlet flow is divided 1:1 between head-neck vessels and descending aorta. A k-ω SST turbulence model with 5% turbulence intensity was used in the simulation.[20] Two cardiac cycles were simulated

to reach stable solution. Blood was modelled as an incompressible, Newtonian fluid with a density of 1060 $kg.m^{-3}$ and dynamic viscosity of 0.0036 $kg.m^{-1}.s^{-1}$.

Analysis

To characterize flow performance, for each of the 8 models, 2 flow dynamic values, known for effects on cardiovascular maladaptation and clinical outcomes, were extracted from CFD: 1) **peak pressure gradient (ΔP)** between the ascending and descending aorta (shown as planes *i* and *ii* in Fig. 2), and 2) **viscous power loss (E_L')**.[22, 23]

The peak pressure gradient at maximal systolic flow rate was calculated through eq 1:

eq 1. $$\Delta P = P_{AAo} - P_{DAo}$$

E'_L was calculated as reported previously:[25]

eq 2. $$E'_L = \mu \sum_{m=1}^{n} \phi_v V_m$$

where:

- $\mu = 0.0036\ kg.m^{-1}.s^{-1}$
- $n = number\ of\ cells$
- $\phi_v = \frac{1}{2}\sum_i \sum_j \left[\left(\frac{\partial v_i}{\partial x_j} + \frac{\partial v_j}{\partial x_i}\right) - \frac{2}{3}(\nabla \cdot v)\delta_{ij}\right]^2\ with\ \delta_{ij} = 1\ for\ i = j\ and\ 0\ otherwise\ (for\ each\ cell)$
- $V_m = volume\ of\ cell\ m$

E'_L represents the viscous power loss in the fluid volume at each point in time. The peak and the average E'_L – calculated as the area under each curve, divided by the period of the cardiac cycle (supplementary material) – were obtained.

For each cardiac function parameter, to compare ΔP and E'_L between the 2 shapes (favorable vs. unfavorable), we also reported the percentage differences of the ΔP or E'_L of the 'low' (-2 SD) shape to the 'high' (+2 SD) shape.

Velocity streamlines and E'_L contours at the time of maximum systolic flow rate, were also generated for all 8 shape modes to visually illustrate the spatial arrangement variabilities within the different geometries.

Results

Table 1 summarizes the peak (systolic) pressure gradients, ΔP, for each geometry. Flows through the 'unfavorable' shapes, i.e. those associated with low LVEF, high iLVEDV, high iLVM and high BP, produced higher pressure gradients (in red) than their 'favorable' counterparts (in green). This corroborated previous phenomenological findings.[17] ΔP reached values between 3.7 and 7.6 mmHg. The highest ΔP highest was seen in the aortic shape linked with high BP (+2SD).

Each shape mode's respective E'_L transient plot is shown in Figure 3. *Highest* (worst) maximum and average E'_L values were seen in aortic shapes associated with low LVEF, high iLVEDV, high iLVM and high BP (Table 2). Percentage differences of the peak values ranged from 9.2% to 26.9%, and the average over a cardiac cycle between 15.1% and 32%. Maximum instantaneous E'_L ranging from 66.90 mW to 91.56 mW, while average E'_L ranging between 10.77 mW and 15.24 mW.

The velocity streamlines in Figure 4 qualitatively show how, given the same input flow conditions, the blood flow distributes differently in response to the specific aortic arch shape. The main differences between favorable and unfavorable shape modes in the E'_L contour plots (Figure 5) can be seen in the descending aorta: the flow, as it travels over the transverse arch, either propagates E'_L from the inner to the outer curvature (seen in the high iLVM case) or courses uniformly round the inner curvature. This is also reflected in the velocity fields, where regions of flow acceleration (turbulence) coincide with higher E'_L. Unfavorable shape modes with E'_L mapped a traversing contour, crossing from the inner to the outer curvature, are observed throughout a cardiac cycle and are associated with worse cardiac functions (low LVEF, high iLVEDV, high iLVM and high BP) (Fig. 3).

176

Discussion

In our 2017 study titled "How Successful is Successful?", we asked two questions: 1) can the 3D shape of an aortic arch, late after CoA repair, be fully and quantitatively accounted for, and 2) is 3D aortic arch shape, in it by itself, associated with better/worse cardiovascular outcomes?[17] The novelty of that study was therefore two-folds: introducing statistic shape modelling (SSM) to fully characterize the 3D properties of the aortic arch in a large cohort of patients, and discovering distinct 3D aortic arch shapes that independently correspond with poorer cardiovascular function. While shedding light on the importance of the aortic shape, that study was descriptive in nature and could not afford a mechanistic insight into *how* differences in shape contributed to outcomes, such as worse ventricular performance and hypertension. In a series of studies using 4D CMR to examine flow characteristics in the aortic arch in various congenital heart diseases, Schaeffer's group observed that flow inefficiencies, characterized by increased viscous energy loss, are associated with both natural and surgically reconstructed aortas, such as those in tetralogy of Fallot and following Norwood-type aortic reconstruction.[13, 22] Nonetheless, these studies did not address aortic arch shape relationships late after CoA repair, nor reported arterial pressures or pressure gradients across an aortic arch. Therefore, we employed well-established CFD methods to uncover the flow dynamic differences, i.e., viscous energy loss and peak pressure gradient, that may underpin the observed relationship between aortic arch shapes and cardiovascular outcomes. Adopting the same cohort of patients who are doing well with no clinically important anatomic arch obstruction late after CoA repair, we identified 2 distinct aortic arch shapes that are associated with +2 and -2 SD values for each cardiovascular parameter. CFD simulations revealed worse viscous energy losses were uniformly present in (unfavorable) aortic arch shapes corresponding with low LV function, more LV dilatation, high LV mass, and worse hypertension. Conversely,

ranging from 3.7 and 7.6 mmHg, peak pressure gradients were not hemodynamically nor clinically significant. Moreover, calculated contour mapping suggests that a more complex propagation of viscous energy loss along the aortic arch into the descending aorta is linked with unfavorable outcomes.

Viscous energy loss is not a familiar nomenclature because it is not a clinically measurable quantity. However, in the fields of fluid mechanics and heat/mass transfer, it signifies the undesirable loss of mechanical energy that powers fluid motion due to viscosity. As a viscous fluid, blood motion can produce friction and shear that will partially convert kinetic and potential energies to viscosity-related energy transfers that becomes permanent, unrecoverable losses to the usable mechanical energy of the system. Therefore, the observed viscous energy loss relationship in this study provides a mechanistic link to the previously reported association between aortic arch and worse cardiovascular outcomes, such as systemic hypertension, long after successful CoA repair. This suggests that specific aortic arch shapes that result in increased viscous energy loss may contribute (in part) to late cardiovascular maladaptation, such as lower LVEF or higher iLVM. Unlike the pronounced kinetic energy loss (reflected by large pressure gradients) caused by significant (re-)stenosis or obstruction that typically mandates intervention, shape-related viscous energy loss in patients with successful CoA repair is subtle but can chronically persist in the background despite acceptable echocardiographic interrogation, or even angiographic assessment. Rather, viscous energy loss will not produce discernible, or even clinically measurable, pressure gradients. This is evident by the underwhelming peak pressure gradients obtained from the CFD simulations. While the impact of high-grade aortic arch obstruction on cardiac function and distal organ perfusion is readily diagnosed, how shape-related chronic viscous energy loss, acting under the radar, contributes to poorer late cardiovascular outcome will require further investigation. It is

likely that viscous energy loss is a part of a larger set of factors, including inherent biological variances/vascular properties/genetic predispositions, that result in increased cardiovascular risks for patients with repaired CoA.

To isolate aortic arch shape as the independent focus of the study, the patient cohort represents those who are clinically well *without* residual anatomic aortic arch obstruction. With peak systolic pressure gradients ranging from 3.7 and 7.6 mmHg in the 8 CFD models, the numerical simulation not only validated our patient selection, but also shed light on the challenges to clinically evaluate and monitor shape-related viscous energy loss. It is worth highlighting that for each aortic arch shape pair, the favorable and unfavorable shapes were separated by 4 standard deviations in clinical outcomes. Despite this wide divide in each of the 4 outcome measures, none of the unfavorable aortic arch shapes produced peak pressure gradients that would have registered clinical concern or mandated intervention. What is clear then is that pressure gradient as the traditional measure of adequacy of aortic arch reconstruction is unable to capture shape-related viscous energy loss because it does not produce sufficiently high flow resistance. While unsupported by the present study, it is possible that shape-related viscous energy loss continuously exerts a subtle and subclinical, but cumulative, long term cardiovascular burden in patients after CoA repair. Or perhaps, rather than promote resistance and pressures, high viscous energy loss reflects exaggerated shear stress contour and/or disorganized wave propagation, two factors known to affect unfavorable ventricular-arterial coupling. [24, 25] Due to this insidious nature, a more robust and life-long follow up within an established adult congenital heart program with regular echocardiograms may be indicated for all patients after CoA repair.

Finally, we are often asked (and rightly criticised for) how the additional insights from this exercise would be useful or actionable clinically, i.e., how would one perform the initial CoA repair to

ensure a favorable aortic arch shape? The answer, we are afraid, is that we do not know. The aortic arch studied here are from a cross-sectional population of patients at a late timepoint from the initial CoA repair. Thus, without the knowledge of what the aortic arch looked like immediately after surgery or at any other interceding timepoints, it is not possible to assess the evolution of the initial aortic arch shape to its late or final appearance. And without such a longitudinal, and patient-specific, understanding of aortic arch transformation with time and growth, it would be purely conjecture, and foolhardy, for us to suggest specific operative technique or surgical modification to the standard CoA repairs. Since the vast majority (>80%) of the cohort had extended end-to-end repair, SSM is unable to reveal specific preoperative patient characteristics, intraoperative techniques or postoperative management that may predict the late appearance of the repaired aortic arch.

Limitations

In this study, the CFD simulations of the 8 aortic arch shape models used the same meshing parameters, uniform boundary conditions, rigid-walled and modeling methods. While patient-specific modeling is currently popular, the application of a uniform boundary condition and simulation parameters in this study is logical to focus on the comparative flow dynamics between different aortic arch shapes. By removing inter-patient variabilities in the CFD simulations, in addition to vastly improving the efficiency of the investigation analysis, differences in both viscous energy loss and peak pressure gradients are singularly attributed to shape variations. It must be acknowledged that since aortic arch shape variations are associated with different cardiovascular functional outcomes, the boundary conditions, such as blood pressure and cardiac output and aortic wall properties, that define each model could not be identical. However, as the scope of study is to uncover mechanistic effects of the aortic arch shape, this study is unable to account for all

patient-specific adaptations, including variations in the aortic wall stiffness and compliance. For similar reasons, we did not adopt a multi-scale approach with closed-loop simulation including linkage with a lumped parameter network model. Such an approach would not provide additional information that is gleaned from the granular details in the CFD models.

Conclusion

The present study builds upon our early work on 3D aortic arch shape to advance an insight into the variable flow dynamics that underpins the association of aortic arch shapes with worse cardiovascular outcomes late after successful aortic coarctation repair. Even in the absence of residual obstruction or clinically important pressure gradients, higher viscous energy losses persist in those aortic arch shapes associated with lower left ventricular ejection fraction and higher end-diastolic volume, left ventricular mass, and resting blood pressure. Future work needs to further the understanding of the mechanism by which the insidious dissipation of viscous energy in aortic arch flow results in cardiovascular maladaptation, and whether mitigating strategies can be discovered to modify this unrelenting liability.

Acknowledgements

The authors are grateful for the present and past support from Leducq Foundatioin, the British Heart Foundation and the FirstRand Foundation.

References

1. Syamasundar RP. Coarctation of the Aorta. Vol 7.; 2005. doi:10.1161/CIRCULATIONAHA.114.008821

2. Tanous D, Bensona LN, Horlick EM. Coarctation of the aorta: Evaluation and management. Curr Opin Cardiol. 2009;24(6):509-515. doi:10.1097/HCO.0b013e328330cc22

3. De Divitiis M, Rubba P, Calabrò R. Arterial hypertension and cardiovascular prognosis after successful repair of aortic coarctation: A clinical model for the study of vascular function. Nutr Metab Cardiovasc Dis. 2005;15(5):382-394. doi:10.1016/j.numecd.2005.08.002

4. Mandell JG, Romanowicz J, Loke YH, Ikeda N, Pena E, Siddiqi U, Hibino N, Alexander ME, Powell AJ, Olivieri LJ. Aortic arch shape after arch repair predicts exercise capacity: a multicentre analysis. Eur Heart J Open. 2023 Dec 26;4(1). doi: 10.1093/ehjopen/oead138. PMID: 38223303; PMCID: PMC10786438.

5. Choudhary P, Canniffe C, Jackson DJ, et al. Late outcomes in adults with coarctation of the aorta. Heart. 2015;101(15):1190-1195. doi:10.1136/heartjnl-2014-307035

6. Olivieri LJ, de Zélicourt DA, Haggerty CM, et al. Hemodynamic Modeling of Surgically Repaired Coarctation of the Aorta. Cardiovasc Eng Technol. 2011;2(4):288-295. doi:10.1007/s13239-011-0059-1

7. Mandell JG, Loke YH, Mass PN, et al. Aorta size mismatch predicts decreased exercise capacity in patients with successfully repaired coarctation of the aorta. J Thorac Cardiovasc Surg. 2021;162(1):183-192.e2. doi:10.1016/j.jtcvs.2020.09.103

8. Quail MA, Segers P, Steeden JA, et al. The aorta after coarctation repair - Effects of calibre and curvature on arterial haemodynamics. J Cardiovasc Magn Reson. 2019;21(1):1-9. doi:10.1186/s12968-019-0540-9

9. Ou P, Mousseaux E, Celermajer DS, et al. Aortic arch shape deformation after coarctation surgery: Effect on blood pressure response. J Thorac Cardiovasc Surg. 2006;132(5):1105-1111. doi:10.1016/j.jtcvs.2006.05.061

10. Ou P, Bonnet D, Auriacombe L, et al. Late systemic hypertension and aortic arch geometry after successful repair of coarctation of the aorta. Eur Heart J. 2004;25(20):1853-1859. doi:10.1016/j.ehj.2004.07.021

11. Ou P, Celermajer DS, Mousseaux E, et al. Vascular Remodeling After "Successful" Repair of Coarctation. Impact of Aortic Arch Geometry. J Am Coll Cardiol. 2007;49(8):883-890. doi:10.1016/j.jacc.2006.10.057

12. Ntsinjana HN, Biglino G, Capelli C, et al. Aortic arch shape is not associated with hypertensive response to exercise in patients with repaired congenital heart diseases. J Cardiovasc Magn Reson. 2013;15(1):1-7. doi:10.1186/1532-429X-15-101

13. Schäfer M, Di Maria MV, Jaggers J, et al. High-degree Norwood neoaortic tapering is associated with abnormal flow conduction and elevated flow-mediated energy loss. J Thorac Cardiovasc Surg. Published online 2021:7-9. doi:10.1016/j.jtcvs.2021.01.111

14. Bruse JL, McLeod K, Biglino G, et al. A non-parametric statistical shape model for assessment of the surgically repaired aortic arch in coarctation of the aorta: How normal is abnormal? Lect Notes Comput Sci (including Subser Lect Notes Artif Intell Lect Notes Bioinformatics). 2016;9534:21-29. doi:10.1007/978-3-319-28712-6_3

15. Cosentino F, Raffa GM, Gentile G, et al. Statistical shape analysis of ascending thoracic aortic aneurysm: Correlation between shape and biomechanical descriptors. J Pers Med. 2020;10(2):1-14. doi:10.3390/jpm10020028

16. Bruse JL, McLeod K, Biglino G, et al. A statistical shape modelling framework to extract 3D shape biomarkers from medical imaging data: Assessing arch morphology of repaired coarctation of the aorta. BMC Med Imaging. 2016;16(1):1-19. doi:10.1186/s12880-016-0142-z

17. Bruse JL, Khushnood A, McLeod K, et al. How successful is successful? Aortic arch shape after successful aortic coarctation repair correlates with left ventricular function. J Thorac Cardiovasc Surg. 2017;153(2):418-427. doi:10.1016/j.jtcvs.2016.09.018

18. Antiga L, Piccinelli M, Botti L, et al. An image-based modeling framework for patient-specific computational hemodynamics. Med Biol Eng Comput. 2008;46(11):1097-1112. doi:10.1007/s11517-008-0420-1

19. Morbiducci U, Ponzini R, Gallo D, et al. Inflow boundary conditions for image-based computational hemodynamics: Impact of idealized versus measured velocity profiles in the human aorta. J Biomech. 2013;46(1):102-109. doi:10.1016/j.jbiomech.2012.10.012

20. Goubergrits L, Riesenkampff E, Yevtushenko P, et al. MRI-based computational fluid dynamics for diagnosis and treatment prediction: Clinical validation study in patients with coarctation of aorta. J Magn Reson Imaging. 2015;41(4):909-916. doi:10.1002/jmri.24639

21. Goubergrits L, Riesenkampff E, Yevtushenko P, et al. Is MRI-Based CFD Able to Improve Clinical Treatment of Coarctations of Aorta? Ann Biomed Eng. 2015;43(1):168-176. doi:10.1007/s10439-014-1116-3

22. Schäfer M, Barker AJ, Jaggers J, et al. Abnormal aortic flow conduction is associated with increased viscous energy loss in patients with repaired tetralogy of Fallot. Eur J Cardio-thoracic Surg. 2020;57(3):588-595. doi:10.1093/ejcts/ezz246

23. Ou P, Celermajer DS, Raisky O, et al. Angular aortic arch leads to enhanced systolic wave reflection, central aortic stiffness, and increased left ventricular mass late after aortic coarctation repair: Evaluation with magnetic resonance flow mapping. J Thorac Cardiovasc Surg. 2008;135(1):62-68. doi:10.1016/j.jtcvs.2007.03.059

24. Moyle KR, Mallinson GD, Occleshaw CJ, et al. Wall shear stress is the primary mechanism of energy loss in the Fontan connection. Pediatr Cardiol. 2006;27(3):309-315. doi:10.1007/s00246-005-0918-3

25. Biglino G, Schievano S, Steeden JA, et al. Reduced ascending aorta distensibility relates to adverse ventricular mechanics in patients with hypoplastic left heart syndrome: Noninvasive study using wave intensity analysis. J Thorac Cardiovasc Surg. 2012;144(6):1307-1314. doi:10.1016/j.jtcvs.2012.08.028

Table 1.

Overview of patient characteristics (BSA = body surface area; TAV = tricuspid aortic valve; BAV = bicuspid aortic valve; fBAV = functionally bicuspid aortic valve; E-E = end-to-end anastomosis; ExtE-E = extended end-to-end anastomosis; LVEF = left ventricular ejection fraction; iLVEDV = indexed left ventricular end-diastolic volume; iLVM = indexed left ventricular mass; BP = systolic resting blood pressure). Lower case *i* indicates parameters indexed to patient BSA.

Variables	*Mean±Standard Deviation*
Number of Patients	53
Age at time of CMR [Years]	22.3±5.6
Height [cm]	170.5±9.5
BSA [m²]	1.83±0.21
Aortic Valve Morphology (TAV/BAV/fBAV)	(21/26/6)
Type of Initial Repair (E-E/ExtE-E/Flap/Patch/Balloon)	(42/1/6/3/1)
LVEF [%]	64.1±7.3
iLVEDV [ml/m²]	78.5±14.6
iLVM [g/m²]	64.1±14.7
BP [mmHg]	130.0±17.1

Table 2.

Maximum pressure gradient (ΔP) between the ascending and descending aorta, and maximum and average viscous energy loss (E'_L), derived from CFD. Green denotes values associated with favorable clinical parameters, red unfavorable. Percentage difference, relative to the unfavorable shape mode is shown. In each geometry the CFD and SSM rankings agree. %Diff = Percentage Difference.

SSM		ΔP at Peak Systolic Flow [mmHg]		Peak E'_L [mW]		Ave E'_L [mW]	
LVEF	Low	6.5	29% Diff	86.8	19% Diff	14.9	32% Diff
	High	**5.0**		**72.8**		**11.3**	
iLVEDV	**Low**	**3.7**	45% Diff	**74.9**	9% Diff	**11.5**	17% Diff
	High	6.8		82.5		13.9	
iLVM	**Low**	**4.7**	4% Diff	**68.0**	25% Diff	**10.9**	29.4% Diff
	High	4.9		91.0		15.4	
BP	**Low**	**4.2**	44% Diff	**67.0**	27% Diff	**11.6**	15% Diff
	High	7.6		91.6		13.6	

Figure Legends

Figure 1: Arch geometries of a cohort of 53 patients following CoA repair and the mean template. Bottom panel represents the 8 extracted 3D shapes corresponding to high (+2SD) and low (-2SD) values of the 4 clinical outcomes. LVEF = Left Ventricular Ejection Fraction, iLVEDV = indexed Left Ventricular End Diastolic Volume, iLVM = indexed Left Ventricular Mass and BP = Systemic Blood Pressure.

Figure 2: An example of geometry process showing shape modes contain information of the arch wall as well as the location and size of the head and neck vessels labelled with 'A'. The processed arch geometry showing the flow extension addition and the imposed inlet volumetric flow rate profile for CFD simulations. The planes used to calculate the pressure gradient are visualised and labelled as *i* and *ii*.

Figure 3: Plots of the viscous power loss in the aorta over a single cardiac cycle for both the 'low' and 'high' shape modes of each case, marked respectively by a blue-solid or orange-dashed line. Higher energy loss values are considered unfavorable. Low LVEF, high iLVM, high BP and high iLVEDV all showed higher peak and average energy losses.

Figure 4: Velocity streamlines at maximum inlet flow rate for each geometry showing the influence of the geometry on the flow field distribution in the different volumes.

Figure 5: Contour plots at the time of maximum viscous power loss (E'_L) illustrating the interaction between arch shape and blood flow impacts how and where the E'_L field establishes. In aortas associated with good cardiac function, E'_L establishes more regularly on the inner curvature of the descending aorta instead of propagating losses towards the centre of the lumen.

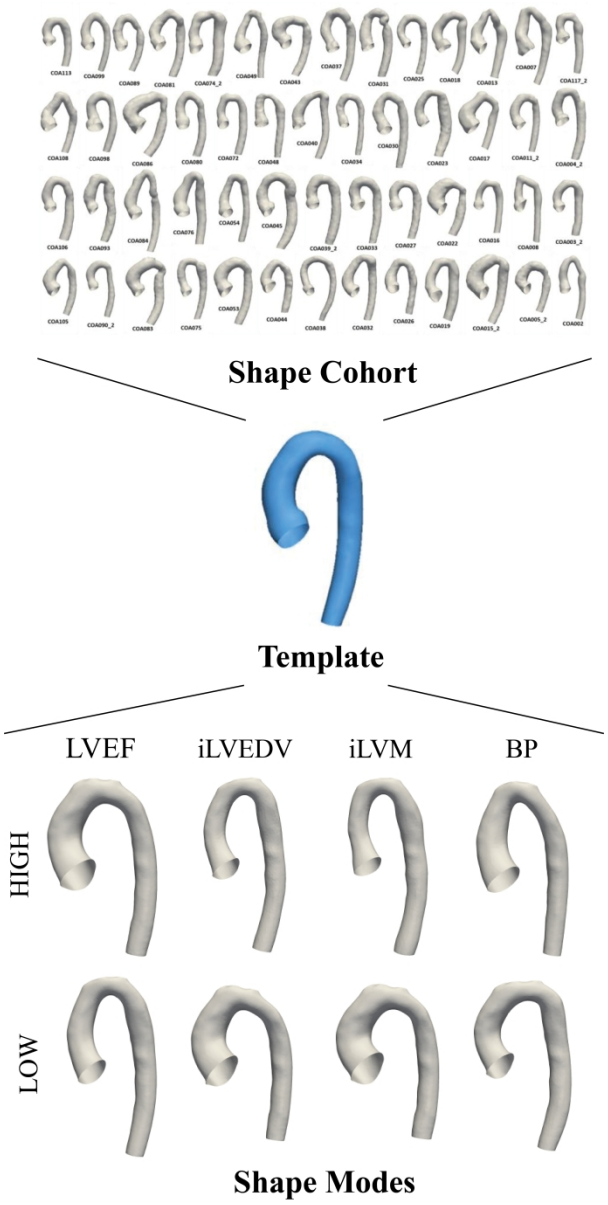

Figure 1: Arch geometries of a cohort of 53 patients following CoA repair and the mean template. Bottom panel represents the 8 extracted 3D shapes corresponding to high (+2SD) and low (-2SD) values of the 4 clinical outcomes. LVEF = Left Ventricular Ejection Fraction, iLVEDV = indexed Left Ventricular End Diastolic Volume, iLVM = indexed Left Ventricular Mass and BP = Systemic Blood Pressure.

79x158mm (1200 x 1200 DPI)

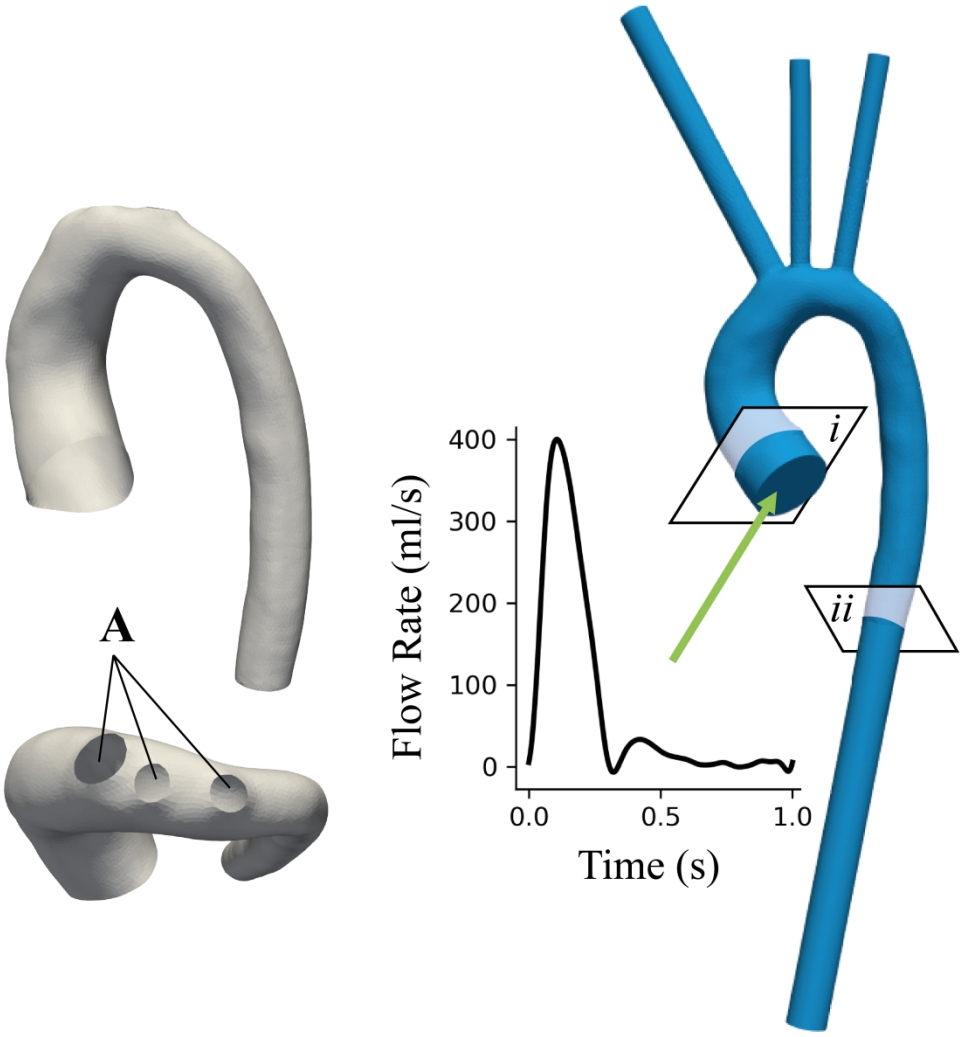

Figure 2: An example of geometry process showing shape modes contain information of the arch wall as well as the location and size of the head and neck vessels labelled with 'A'. The processed arch geometry showing the flow extension addition and the imposed inlet volumetric flow rate profile for CFD simulations. The planes used to calculate the pressure gradient are visualised and labelled as i and ii.

83x87mm (1200 x 1200 DPI)

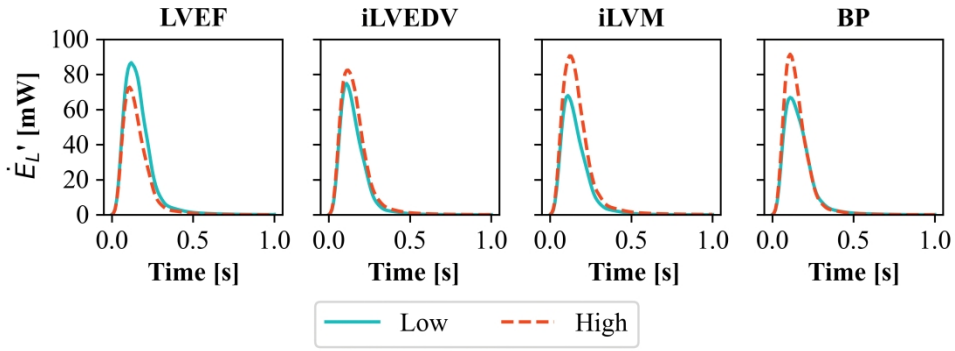

Figure 3: Plots of the viscous power loss in the aorta over a single cardiac cycle for both the 'low' and 'high' shape modes of each case, marked respectively by a blue-solid or orange-dashed line. Higher energy loss values are considered unfavorable. Low LVEF, high iLVM, high BP and high iLVEDV all showed higher peak and average energy losses.

406x152mm (236 x 236 DPI)

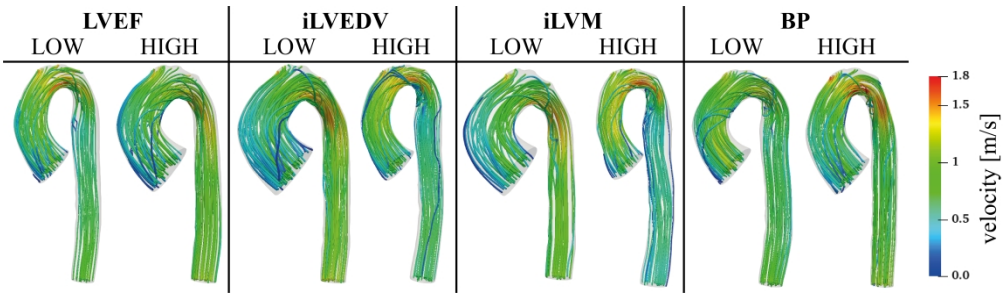

Figure 4: Velocity streamlines at maximum inlet flow rate for each geometry showing the influence of the geometry on the flow field distribution in the different volumes.

458x131mm (472 x 472 DPI)

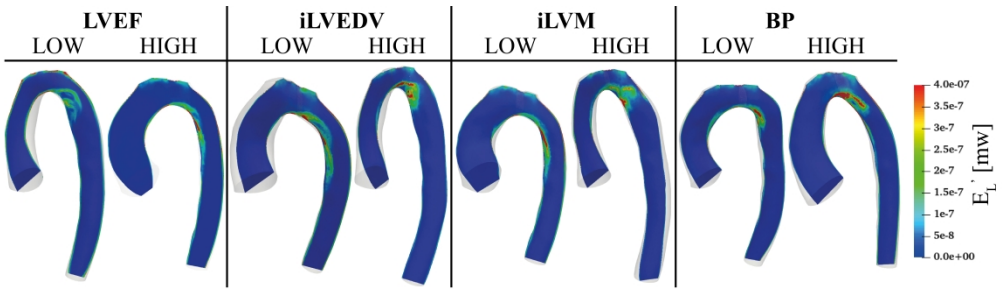

Figure 5: Contour plots at the time of maximum viscous power loss (E_L^') illustrating the interaction between arch shape and blood flow impacts how and where the E_L^' field establishes. In aortas associated with good cardiac function, E_L^' establishes more regularly on the inner curvature of the descending aorta instead of propagating losses towards the centre of the lumen.

464x131mm (472 x 472 DPI)

Supplementary Material

S.1. Mesh Independence Study

Meshing

A mesh independence study was conducted on the iLVM High geometry shown in Supplemental Figure 1 A due to the challenging haemodynamic environment – as compared to other geometries – created by its narrow ascending aorta, short transverse arch, and the dilation in the descending aorta. As a result, the mesh settings which achieved mesh independence for this geometry would suffice, if not be conservative, for the rest of the geometries. To this end, six meshes comprising 120k to 6.2M cells were generated where each consecutively refined mesh approximately doubled the number of cells.

The commercial ANSYS (v20.0) ICEM CFD mesh generator was used. The domain was discretised using a combination of tetrahedral and prism type cells. The cell size of the boundary layer (BL) prisms was based on the global maximum cell size defining each level of refinement and did not utilise any local, curvature or proximity-based refinement strategies. The parameters defining the layers of this region (highlighted in Supplemental Figure 1 A) was chosen, through iterations, so that the maximum y^+ value at the wall was approximately 1. The required parameters were:

Boundary Layer Height: 1mm

Number of Layers: 10

Growth Ratio: 1.2

Mesh Independence Metrics

Mesh independence was defined as a change of <2% in the metric measured between the mesh being considered (m_x) and the finest mesh (m_{ref}) which was considered as the reference. The metrics used were:

1. The average difference between centreline pressures on m_x and m_{ref} compared to the maximum value of pressure on the m_{ref} centreline (eq. 1). Pressures along the centreline were calculated as the area-weighted average across 54 cross-sections of the aorta spanning the region between planes *i* and *ii* in Supplemental Figure 1 (B). The calculation did not include any of the flow extensions since these would not be considered in the analysis. The resulting planes are shown in Figure 1 C.

eq 1. $$\%P_{CL} = 100 \times \left| \frac{\frac{1}{54}\sum_{i=1}^{54}\left(P_x^i - P_{ref}^i\right)}{P_{ref}^{max}} \right|$$

2. The percentage change in volumetric flow rate at plane *ii* seen in Figure 1 (B) relative to that of m_{ref}, as calculated in eq 2.

eq 2. $$\%Q_{DAo} = 100 \times \left| \frac{Q_x^{DAo} - Q_{ref}^{DAo}}{Q_{ref}^{DAo}} \right|$$

3. The percentage change in volume averaged velocity magnitude across the entire fluid domain, including flow extensions, relative to that of m_{ref}, as calculated through eq. 3.

eq 3. $$\%\bar{v} = 100 \times \left| \frac{\bar{v}_x - \bar{v}_{ref}}{\bar{v}_{ref}} \right|$$

CFD Modelling Method for Mesh Independence:

Peak systolic flow conditions were modelled using a steady-state solver. Fluid modelling parameters and boundary conditions are listed below:

Inlet Velocity Boundary Condition:	Parabolic velocity profile with $v_{max} = 1.08996\ m/s$ to correspond to a volumetric flow rate of 400 ml/s
Outlet Boundary Condition:	Zero-pressure
Turbulence Model:	kω-SST with 5% turbulence intensity at the inlet
Blood Density:	1050.0 kg/m^3
Blood Viscosity:	0.0036 Pa·s with a Newtonian Fluid Assumption
Solver Algorithm:	SIMPLEC
Discretisation Schemes:	Second Order for Momentum and Pressure; First Order for Turbulent Kinetic Energy and Specific Dissipation Rate
Convergence Criteria:	1e-4 for residuals of volume average velocity and pressure and 1e-3 for velocity vector components.

Results:

The area-weighted average pressure on 54 cross-sectional slices along the centreline spanning the region of interest, shown in Supplemental Figure 1 C, is plotted for each mesh in Supplemental Figure 2. The average difference along the entire centreline, compared to the maximum pressure value on m_{ref} mesh was calculated and found to be <2% at the fourth level of refinement where the cell count was approximately 1.9M cells. This is seen by it being lower than the threshold – indicated as a dashed grey line – in Supplemental Figure 3.

The analysis of the additional metrics of volume averaged velocity and descending aorta (DAo) volumetric flow rate both showed convergence at the second and third level of refinement, respectively, as seen in Supplemental Figure 3.

Considering all three metrics together, the numerical results were found to be adequately independent at the fourth level of refinement where the cell count reached ~1.9M cells. The meshing parameters of this mesh were then used to generate meshes of the remaining geometries.

The final meshing parameters used were:

Global Maximum Cell Size: 1.16 mm

Cell Types: Tetrahedral for lumen region; triangular prisms in BLs adjacent to the wall

Local Refinement Strategy: Uniform Meshing

Boundary Layer Height: 1 mm

Number of Layers: 10

Growth Ratio: 1.2

S.2. Boundary Layer E_L' Study

Background

Earlier studies by Schafer et al. and Barker et al. calculated viscous power loss (E_L') from phase-contrast cardiac MRI flow maps of patients with tetralogy of Fallot and aortic valve stenosis.[1,2] The study by Barker et al. specifically excluded E_L' in the near wall voxels so that internal flow features, which were of primary interest, were characterised.[2] The resulting values of E_L' from these pieces of literature, which included healthy and diseased patients, reached ~30 mW, in individual cases, although the cohort average in Schafer et al. was found to be lower at about 4 mW.[1] By ignoring the E_L' in the near wall region, where the viscous sublayer of flow exists, the method in the above pieces of literature likely underestimates E_L'. However, it cannot be said to what extent pathological E_L' differs from a healthy patient, due to the current lack of a definitive baseline for healthy E_L'.

The calculation of E_L', using eq 4, relies solely on the velocity gradients within the flow field which are expected to be high near the wall due to the zero slip flow condition applied at the wall.[3] Furthermore, the resolution to which these gradients are resolved is critical and it may be that the coarse resolution of MRI underestimates the E_L' in the domain. This highlights a benefit of CFD analysis which may complement the MRI studies through its arbitrarily high resolution to capture full E_L'.

eq 4. $$E_L' = \mu \sum_{m=1}^{n} \phi_v V_m$$

where:

- $n = number\ of\ voxels\ or\ cells$
- $\phi_v = \frac{1}{2}\sum_i \sum_j \left[\left(\frac{\partial v_i}{\partial x_j} + \frac{\partial v_j}{\partial x_i}\right) - \frac{2}{3}(\nabla \cdot v)\delta_{ij}\right]^2 \quad (for\ each\ voxel)$
- $\delta_{ij} = 1\ for\ i = j\ and\ 0\ otherwise$

In this study the contribution of the boundary layer (BL) E_L' became evident when the CFD derived E_L' values were significantly higher than the range expected from Schafer et al. [1] and Barker et al. [2]. In our study the peak E_L' values reached as high as 90 mW. Upon further inspection, the flow domain showed E_L' to be dominant in the BL region. To quantify this, E_L' was summed over the domain, first including the BL cells and then excluding them and were plotted over the cardiac cycle. The percentage contribution by E_L' in the BL cells was then calculated and reported in Supplemental Table 1.

Results and Discussion

Supplemental Figure 4 qualitatively presents E_L' at various cross-sections of the domain and highlights a predominance of E_L' in the BL. The contribution is significant and can be seen in Supplemental Figure 5 by the difference between the solid and dashed lines which represent the calculations with BLs (W/BL) and without (WO/BL), respectively. The peak of the E_L', which excluded the BL region, reached values of order of magnitude of 10 mW which aligns closer to the results of Schafer et al. and Barker et al.[1.2] The quantitative analysis presented in Supplemental Table 1 found that, in general, circa 90% of E_L' was attributed to the near-wall region of flow both at peak power loss and on average over the cycle. Once excluded, the values in the domain reduced to what was more in line with results reported by previous literature.

Although there is this significant reduction in E_L' when excluding the BL region, the overall ranking of the geometries does not change, as compared to the results reported in the main manuscript. This emphasises the comparative nature of this work and affirms the results of the main study.

Supplemental References

1. Schäfer M, Barker AJ, Jaggers J, et al. Abnormal aortic flow conduction is associated with increased viscous energy loss in patients with repaired tetralogy of Fallot. Eur J Cardio-thoracic Surg. 2020;57(3):588-595. doi:10.1093/ejcts/ezz246

2. Barker AJ, Van Ooij P, Bandi K, et al. Viscous energy loss in the presence of abnormal aortic flow. Magn Reson Med. 2014;72(3):620-628. doi:10.1002/mrm.24962

3. Bird RB. Transport Phenomena. Vol 1.; 1980.

Table 1: Tabulated calculations of E_L' in the boundary layers alone and a comparison of the proportion of total E_L' in the domain. It was found that the E_L' in the boundary layers generally comprised ~90% of the total E_L' in the domain both at the peak E_L' and on average.

MAX EL DIFFERENCE				
SSM		**Total E_L' (Maximum) [mW]**	**BL Contribution [mW]**	**%Diff**
EF	Low	86.8	78.6	90.6
	High	72.8	67.7	93.0
iLVM	Low	68.0	62.8	92.4
	High	90.6	81.9	90.3
BP	Low	66.9	60.7	90.8
	High	91.6	83.8	91.5
iLVEDV	Low	74.9	69.5	92.8
	High	82.5	74.8	90.8
AVERAGE EL DIFFERENCE				
SSM		**Total E_L' (Average) [mW]**	**BL Contribution [mW]**	**%Diff**
EF	Low	14.9	13.3	89.3
	High	11.3	10.2	90.2
iLVM	Low	10.9	9.7	89.3
	High	15.4	13.6	88.6
BP	Low	11.6	10.2	88.5
	High	13.6	12.2	89.2
iLVEDV	Low	11.5	10.4	89.9
	High	13.9	12.4	88.8

Supplemental Figure Legends

Supplemental Figure 1: A: Visualisation of the geometry after flow extensions along with a view of an example of the boundary layers and mesh. B: planes i and ii show the limits of the geometry before flow extensions were added. The vessel centreline between these planes was generated and 54 cross-sectional planes were generated along the centreline between these planes. C: The cross-sectional slices generated to determine mesh independence.

Supplemental Figure 2: Area-weighted average static pressure at 54 cross-sections, along the centreline of the aortic arch. The coarsest mesh shows the largest differences with the finest mesh and as the mesh refinement increases the pressure results converged to the same result.

Supplemental Figure 3:Mesh independence was measured on three metrics namely: the flow rate through the descending aorta, the volume averaged velocity and the pressure measured along the centreline of the aorta. The metrics were measured relative to the fines mesh and when the difference fell below 2%, the domain was considered sufficiently discretised. This was found at the fourth level of refinement.

Supplemental Figure 4: Peak E_L^' field highlighting the predominance of E_L^' in the boundary layer region adjacent to the wall.

Supplemental Figure 5: Plots showing the cumulative viscous energy loss in the aortic arch, over the cardiac cycle, in the different cell zones of each geometry. Solid lines indicate the E_L^' in both the tetrahedral and prism boundary layers (W/BL = with boundary layer) whereas the dotted lines show the E_L^' in just the tetrahedral cells (WO/BL = without boundary layer). The difference between the lines indicates the E_L^' in the boundary layer cells alone.

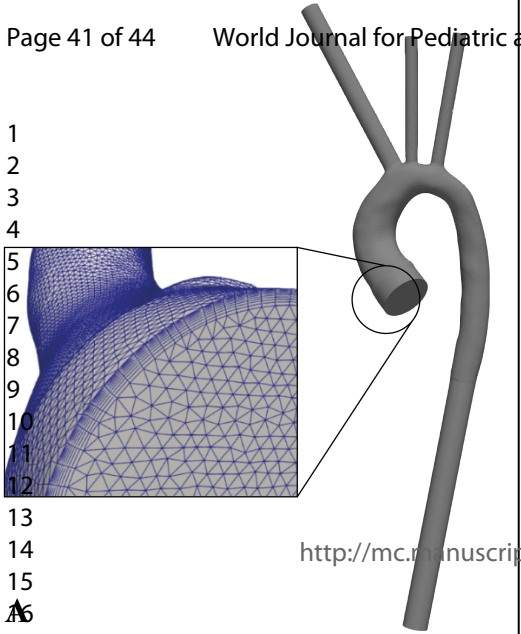

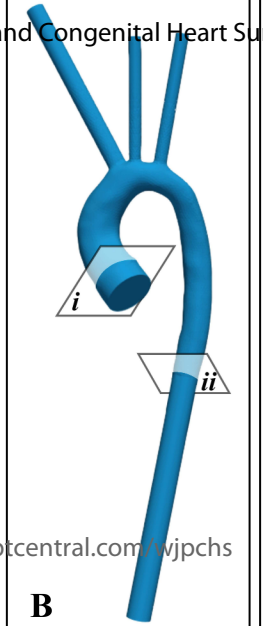

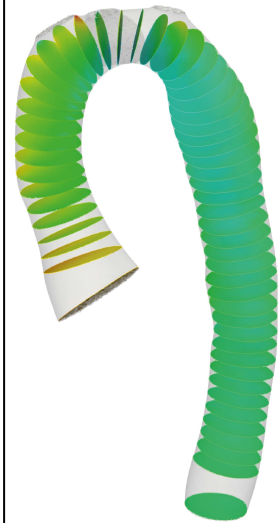

A B C

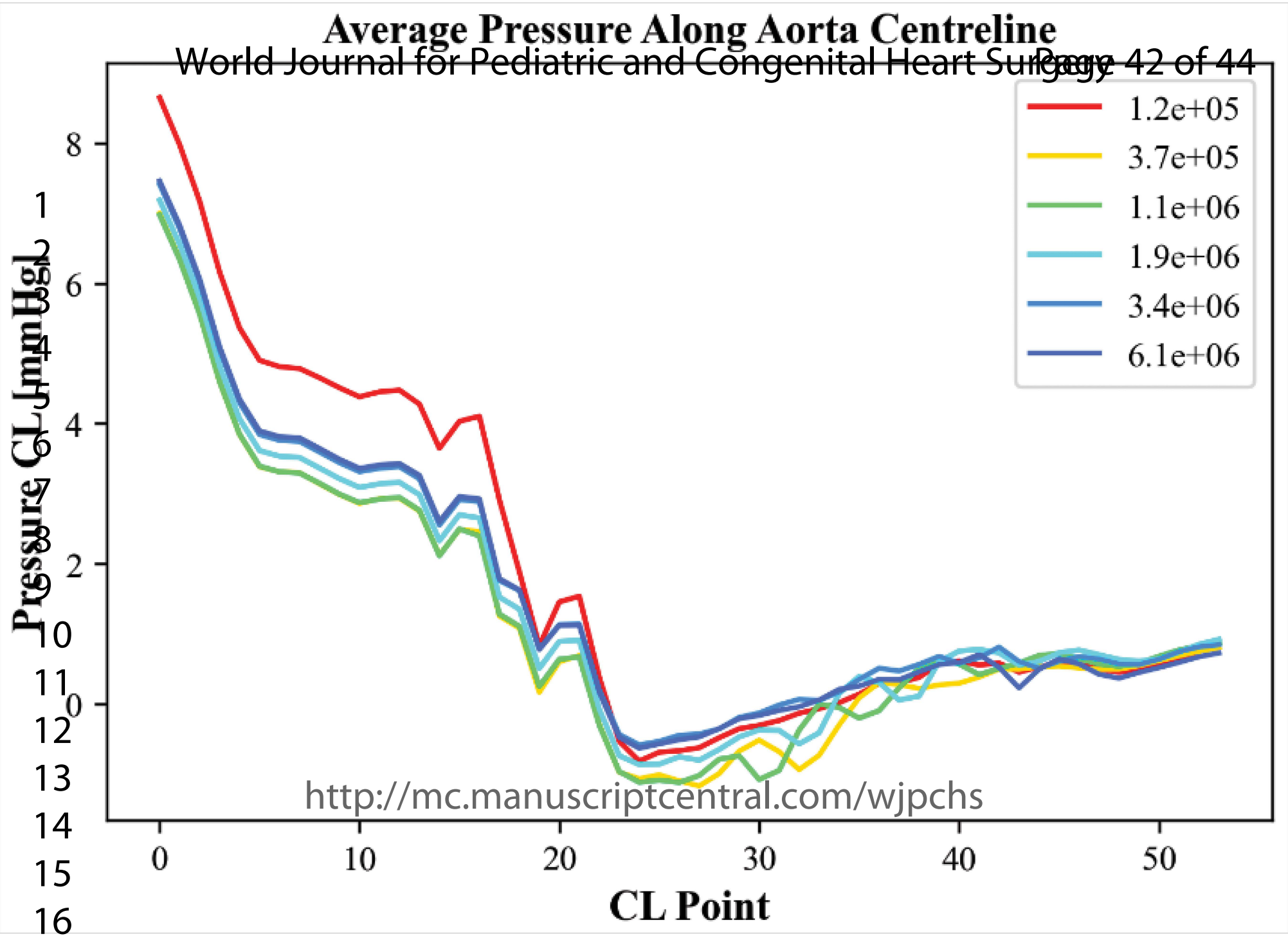
Average Pressure Along Aorta Centreline
1.2e+05
3.7e+05
1.1e+06
1.9e+06
3.4e+06
6.1e+06
Pressure CL [mmHg]
CL Point
0
10
20
30
40
50
http://mc.manuscriptcentral.com/wjpchs